Characterization of neurite and soma organization in the brain and spinal cord with diffusion MRI

Kurt G Schilling[1,2*], Marco Palombo[3,4], Atlee A. Witt[1], Kristin P. O'Grady[1,2,5], Marco Pizzolato[6], Bennett A Landman[1,2,5,7] , Seth A. Smith[1,2,5]

1. Vanderbilt University Institute of Imaging Science, Vanderbilt University Medical Center, Nashville, TN, United States
2. Department of Radiology and Radiological Sciences, Vanderbilt University Medical Center, Nashville, TN, United States
3. CUBRIC, School of Psychology, Cardiff University, Cardiff, UK
4. School of Computer Science and Informatics, Cardiff University, Cardiff, UK
5. Department of Biomedical Engineering, Vanderbilt University, Nashville, TN, United States
6. Department of Applied Mathematics and Computer Science, Technical University of Denmark, Kgs. Lyngby, Denmark
7. Department of Electrical Engineering and Computer Engineering, Vanderbilt University, Nashville, TN, USA
*corresponding author: kurt.g.schilling.1@vumc.org

Abstract

The central nervous system (CNS), comprised of both the brain and spinal cord, and is a complex network of white and gray matter responsible for sensory, motor, and cognitive functions. Advanced diffusion MRI (dMRI) techniques offer a promising mechanism to non-invasively characterize CNS architecture, however, most studies focus on the brain or spinal cord in isolation. Here, we implemented a clinically feasible dMRI protocol on a 3T scanner to simultaneously characterize neurite and soma microstructure of both the brain and spinal cord. The protocol enabled the use of Diffusion Tensor Imaging (DTI), Standard Model Imaging (SMI), and Soma and Neurite Density Imaging (SANDI), representing the first time SMI and SANDI have been evaluated in the cord, and in the cord and brain simultaneously. Our results demonstrate high image quality even at high diffusion weightings, reproducibility of SMI and SANDI derived metrics similar to those of DTI with few exceptions, and biologically feasible contrasts between and within white and gray matter regions. Reproducibility and contrasts were decreased in the cord compared to that of the brain, revealing challenges due to partial volume effects and image preprocessing. This study establishes a harmonized approach for brain and cord microstructural imaging, and the opportunity to study CNS pathologies and biomarkers of structural integrity across the neuroaxis.

Keywords: Diffusion MRI, Brain, Spinal Cord, In Vivo, Microstructure, Soma, Neurites

Introduction

The central nervous system (CNS), comprised of both the brain and spinal cord, is a highly interconnected network that facilitates a range of sensory, motor, and cognitive functions (Nieuwenhuys et al., 2008). The CNS is composed of two main types of tissue, white matter (WM) and gray matter (GM). White matter is made up of a network of nerve fibers (i.e., myelinated axons) that facilitate communication between areas of the brain and spinal cord, while the gray matter is composed of neuronal cell bodies (i.e., soma) and dendrites responsible for processing and integrating neural information (Felten, 2021) (**Figure 1**). The brain and cord are highly interconnected, and any changes in the organization and microstructure in one region, such as the brain, could propagate and impact the structure and function of the spinal cord, or vice-versa. Therefore, it is crucial to examine both structures together when studying anatomy or pathology of the CNS. In this study, we aim to characterize the microstructural organization of both the brain and spinal cord using clinically feasible diffusion MRI (dMRI), identifying what aspects of tissue microstructure can be reliably detected and characterized in both regions.

Diffusion MRI has proven to be a powerful tool to study the microstructural organization of the CNS (Beaulieu, 2002; Le Bihan & Iima, 2015). Several signal representations and microstructural models have been developed and applied to study CNS in health and disease (Novikov, Fieremans, et al., 2018; Novikov, Kiselev, et al., 2018) (**Figure 2**). Among the earliest, diffusion tensor imaging (DTI) (Basser et al., 1994; Pierpaoli et al., 1996) captures the anisotropic diffusion of water in tissue as a (covariance matrix of a) 3D Gaussian distribution (**Figure 2, top**). From DTI, scalar indices of diffusivity can be derived including axial (AD), radial (RD), and mean diffusivities (MD), as well as indices of orientation anisotropy like fractional anisotropy (FA) (Pierpaoli et al., 1996). Acquisition requirements for DTI analysis are not relatively demanding, requiring only ~15-30 diffusion-weighted images with a single b-value shell (typically b~1000s/mm2), conditions that are readily achievable on clinical scanners (Jones & Cercignani, 2010; Jones et al., 1999). Because of this, DTI has been applied extensively in both the brain (Mori & Zhang, 2006) and spinal cord (Vedantam et al., 2014) to study injury, neurological disease, and developmental processes in both WM and GM tissues. While DTI-based indices sensitively reflect tissue properties, such as myelination and fiber density (Beaulieu, 2002), they lack specificity and are confounded by orientation and partial volume effects (Jones & Cercignani, 2010).

To overcome this limited specificity, several multi-compartmental approaches have been developed to explicitly model certain aspects of the tissue environment (Novikov, Fieremans, et al., 2018; Novikov, Kiselev, et al., 2018). Among others (Jelescu, Veraart, et al., 2016; Jespersen et al., 2007; Kroenke et al., 2004; Novikov, Veraart, et al., 2018; Reisert et al., 2014; Sotiropoulos et al., 2012), models such as neurite orientation dispersion and density imaging (NODDI) (Zhang et al., 2012), multi-compartment spherical mean technique (SMT) (Kaden, Kelm, et al., 2016; Kaden, Kruggel, et al., 2016), or White Matter Tract Imaging (WMTI) (Fieremans et al., 2013; Fieremans et al., 2011), have become popular in both the brain and spinal cord because they can be employed using a clinically

feasible two-shell (two b-values) acquisition. While there are unique differences in constraints, assumptions, and derived indices, many of these models fall under the umbrella of the so-called *Standard Model* of neuronal tissue (Novikov, Fieremans, et al., 2018). In Standard Model Imaging (SMI) (**Figure 2, middle**), axons are represented as impermeable zero-radius sticks arranged in coherent bundles and embedded within an extra-axonal space described by an axially symmetric diffusion tensor, along with a third cerebral spinal fluid (or free water) compartment. Thus, SMI results in indices of axonal (or signal) fraction (f), along-axon diffusivity (D_a), extra-axonal parallel ($D_e^{\parallel}$) and perpendicular ($D_e^{\perp}$) diffusivities, free water (signal) fraction (f_w), and a measure of fiber dispersion (p_2). These indices have been shown to be highly specific to normal anatomical variation (Coronado-Leija et al., 2024) and disease processes such as demyelination ($D_e^{\perp}$) (Fieremans et al., 2012; Jelescu, Zurek, et al., 2016), axonal loss (f) (Fieremans et al., 2012), and axonal beading (D_a) (Lee et al., 2020), with reproducible and robust estimates on clinical scanners (Coelho et al., 2022). However, SMI has not yet been demonstrated in the spinal cord, where descriptions of normal variation and reproducibility could well-compliment the same measures derived in the brain. Additionally, the standard model is based on geometrical assumptions specific to white matter and may not be entirely appropriate for gray matter tissue.

More recently, the Soma and Neurite Density Imaging (SANDI) model (Palombo et al., 2020) has emerged as a promising technique for studying both white matter and gray matter architecture in the CNS. By distinguishing between water diffusion within neurites (stick-like axons and dendrites) and soma (spherical neuronal cell bodies), SANDI provides a more comprehensive characterization of tissue microstructure than previously mentioned models, extending the standard model to also include soma fraction (f_{soma}) and soma radii (R_{soma}) estimates (**Figure 2, bottom**). However, this comes at the cost of a significantly increased scan time, requiring a minimum of 5 diffusion shells, with b-values 6-10x higher than those typical of clinical acquisitions. In the original paper (Palombo et al., 2020), the SANDI model was fit on data with b-values up to 10,000s/mm^2 acquired on a high-performance scanner, showing white and gray matter contrasts that paralleled those obtained from myelo-architectural and cyto-architectural stains. More recently, Genc et al., (Genc et al., 2021) revealed that these maps were highly repeatable and reproducible using much lower b-values of b=6000s/mm^2, but still acquired using high performance systems. Finally, Schiavi et al. (Schiavi et al., 2023) demonstrated the feasibility of acquiring SANDI metrics on a clinical scanner, highlighting biases due to noise and acquisition schemes, but resulting in reliable and reproducible measures in both white and gray matter. However, again, these were demonstrated in the brain, and feasibility of SANDI modeling has not been done on the cord.

Motivated by these works in the brain, and the desire to study both the brain and spinal cord in parallel with a harmonized acquisition, we aim to characterize neurite and soma organization in the brain and spinal cord using diffusion MRI on a clinical scanner. In agreement with existing literature, we show that DTI, SMI, and SANDI are feasible, reproducible, and result in biologically meaningful measures of the brain, but address

challenges in image acquisition and image processing (Cohen-Adad et al., 2021; Kurt G Schilling et al., 2021) to demonstrate similar application of these models in the cord. We first describe the acquisition which enables application of these models in the gray and white matter, then show and assess data quality and resulting indices in both the brain and cord. Next, we assess reliability and repeatability of these models, and finally compare model indices to known anatomy and expected contrast within and between white and gray matter tissues.

Methods

Brain and Cord - acquisition

Eleven healthy controls participated in this study, with six scanned twice for scan-rescan reproducibility assessment. All experiments were performed on a 3.0T whole body MR scanner (Philips dStream Ingenia, Best, Netherlands). A two-channel body coil was used for excitation and a 16-channel SENSE neurovascular coil was used for reception. The maximum gradient strength of the system was 80 mT/m at a slew rate of 100 mT/m/s. All data were acquired under a protocol approved by the local institutional review board (IRB #111087) and informed consent was obtained prior to the study.

Brain imaging consisted of a T1-weighted image using a three-dimensional (3D) T1-MPRAGE image (TR=6.3ms, inversion time = 1060ms, TE = 2.9ms, flip angle 8 degrees, spatial resolution 1x1x1mm3, acquisition time = 5m37s). The diffusion protocol consisted of a pulsed-gradient spin-echo sequence with single-shot echo planar imaging (EPI) readout with the following parameters: repetition time 4400 ms, echo time 100 ms, pulse duration 24 ms, pulse separation 60 ms, spatial resolution 2.5 x 2.5 x 2.5mm3, 62 slices, whole-brain coverage, axial orientation, SENSE=2.2, Multiband=2, partial Fourier =0.70, with 7 (non-zero) b-values of 0/100/500/1000/2000/3000/4000/6000 with 22/8/8/16/24/32/40/48 measurements per shell, acquired with phase encoding in the anterior-posterior direction, with a scan of 6 b=0s/mm2 images with reversed phase encoding. The total scan time for brain diffusion data was 16.5 minutes. We note that the sequence was separated into three sequential acquisitions, with constant pre-scan settings, because the software did not allow >128 diffusion-weighted volumes in a single acquisition. Scans were simply concatenated prior to preprocessing (*mrcat* from MRTrix3 (Tournier et al., 2019) tools).

Cord imaging consisted of a high-resolution (0.65 × 0.65 × 5 mm³) multi-slice, multi-echo gradient echo (mFFE) anatomical image (Held et al., 2003)
(TR/TE/ΔTE = 753/7.1/8.8 ms, α = 28°, number of slices = 14, 6:12 min) for co-registration and to serve as a reference image for segmentation. The diffusion protocol was matched to the brain, and consisted of a pulsed-gradient spin-echo sequence with single-shot EPI readout with the following parameters: repetition time 4400 ms, echo time 100 ms, pulse duration 24 ms, pulse separation 51 ms, spatial resolution 1.1 x 1.1 x 5mm3, 18 slices, axial orientation, SENSE=1.8, Multiband=None, partial Fourier = 0.69, with 7 (non-zero) b-values of 0/100/500/1000/2000/3000/4000/6000 with 22/8/8/16/24/32/40/48 gradient directions performed per shell, acquired with phase encoding in the left-right direction,

with a scan of 6 b=0s/mm2 images with reversed phase encoding. All images were centered at the C3/C4 intervertebral disc. Reduced field-of-view was applied using an outer volume suppression technique (Wilm et al., 2007) and fat suppression was achieved using SPIR. The acquisition was not cardiac triggered in order maximize acquisition per time (Kurt et al., 2023). The total scan time for cord diffusion data was 16.5 minutes. Again, the sequence was separated into three sequential acquisitions, with constant pre-scan settings, and concatenated prior to preprocessing.

Data is made available in BIDS format in the Zenodo sharing platform (https://doi.org/10.5281/zenodo.15512428).

Brain and Cord - Preprocessing

Brain data preprocessing started with running FreeSurfer 6.0 (Fischl, 2012; Fischl et al., 2002) in order to derive 24 regions-of-interest (ROIs) from the lobe-based parcellation including 12 gray matter labels (bilateral Frontal, Parietal, Occipital, Temporal, Cingulate, Subcortical) and the corresponding 12 white matter labels. The diffusion dataset was preprocessed using a combination of FSL (6.0.7.9) (Jenkinson et al., 2012) and MRTrix3 software (Tournier et al., 2019), and included MPPCA denoising (Veraart, Novikov, et al., 2016), Gibbs-Ringing correction (Kellner et al., 2016), and correction of motion, eddy currents, and susceptibility distortion(Andersson et al., 2003; Andersson et al., 2016), followed by a final round of denoising using Patch2Self (Fadnavis et al., 2020), which can be applied at any point in the preprocessing pipeline. Noise maps were estimated from the MPPCA denoising process.

Spinal cord data preprocessing utilized tools from the Spinal Cord Toolbox (v6.2) (De Leener et al., 2017). Preprocessing started with vertebral labelling (*sct_label_vertebrae*) (Ullmann et al., 2014) on the structural mFFE and subsequent registration (*sct_register_to_template*) to the PAM50 template (De Leener et al., 2018). From this regions of interest were defined within cervical levels 3 (C3) and 4 (C4). For each of these two levels, 12 distinct ROIs were defined: 6 in gray matter (consisting of bilateral Ventral Horns, Intermediate Zones, and Dorsal Horns) and 6 in white matter (bilateral Dorsal Columns, Lateral Columns, and Ventral Columns). This resulted in a total of 24 ROIs across C3 and C4. Diffusion preprocessing included MPPCA denoising (Veraart, Fieremans, et al., 2016), Gibbs-Ringing correction (Kellner et al., 2016), motion correction (using SCT *sct_dmri_moco* (Xu et al., 2013) including slice-wise regularized registration along the SI-axis, iterative averaging of the target volumes, and group-wised alignment of DWIs with grouping g=8), followed by Patch2Self denoising (Fadnavis et al., 2020). Noise maps were estimated from the MPPCA denoising process. For region-wise metric extraction, a maximum a posteriori method was used to mitigate partial volume effects (Lévy et al., 2015) (*sct_extract_metric*).

All data was quality checked at every point in the process, with manual inputs to vertebral alignment, masking, and alignment parameters if needed.

Microstructure Modeling

The DTI, SMI, and SANDI models were fit to the preprocessed data for both brain and cord.

DTI was fit using FSL toolbox command *dtifit,* using only b-values b<=2000 (b=100, 500, 1000, 2000) and simultaneously fitting both the Diffusion and Kurtosis tensors (Jensen et al., 2005) using linear least squares on the log-transformed signal. This resulted in maps of FA, MD, AD, and RD, describing the degree of diffusion anisotropy, the mean of the three eigenvalues of the diffusion tensor, the diffusion parallel to the principal diffusion direction, and the diffusion perpendicular to the principal diffusion direction, respectively. Finally, from the kurtosis tensor (Jensen et al., 2005), the mean kurtosis (MK) describing the average of the diffusion kurtosis along all directions. Kurtosis describes non-Gaussianity of the diffusion process and has been interpreted as a more complex diffusion pattern within the imaging voxel (due to hindrances and restrictions).

SMI fitting was performed using the Standard Model Imaging Matlab toolbox (https://github.com/NYU-DiffusionMRI/SMI; 998a4c2 release) (Coelho et al., 2022) providing b-values b<=3000 (b=100, 500, 1000, 2000, 3000) and the estimated noise map for Rician bias correction prior to fitting. This toolbox used root-mean-squared error (RMSE) machine-learning based estimators for parameter estimation (Reisert et al., 2017). This resulted in maps characterizing intracellular space including axonal fraction (f) describing the relative signal contribution of intra-axonal space, intra-axonal diffusivity (D_a) along axons, and orientational coherence parameter (p_2). Maps characterizing extracellular space included the radial diffusivity ($D_e^{\perp}$) and axial diffusivity ($D_e^{\parallel}$). And finally, the free water fraction (f_w) describing the signal fraction of an isotropic free water component.

To fit the SANDI model we used the SANDI Matlab Toolbox (https://github.com/palombom/SANDI-Matlab-Toolbox-Latest-Release; 67d599c release), using as input the respective preprocessed diffusion data and noise maps for the brain and cord. The toolbox similarly uses machine-learning based estimators for parameter estimation. We fixed the intra-soma diffusivity to 3 um²/ms, and upper bounds for D_{in} and D_e to 3 um²/ms, and soma radius upper bound automatically set by default to a maximum value given the diffusion time and intra-soma diffusivity.

Analysis

To evaluate image quality, the apparent signal-to-noise ratio (SNR) (the SNR after the adopted image preprocessing) was calculated following (Schiavi et al., 2023), using two consecutive b=0 images:

$$SNR = \frac{1}{\sqrt{2}} \frac{mean_{ROI}(S_1(b=0) + S_2(b=0))}{std_{ROI}(S_1(b=0) - S_2(b=0))}$$

where S1 and S2 are the first two consecutive b=0 images. The SNR was calculated in three regions-of-interest (ROIs), including white matter, gray matter, and their sum, for both the brain and spinal cord.

The reliability of each diffusion metric, for all models, in both the brain and cord, was evaluated using the three commonly used statistical measures in medical imaging (Palombo et al., 2023; Schiavi et al., 2023; Schiavi et al., 2022; Veraart et al., 2021): Pearson correlation r, the test-retest variability (TRV), and intraclass correlation coefficient (ICC). The Pearson correlation r was computed using the MatLab *corrcoeff* function using

the test-retest values of the 24 brain ROIs (12 WM and 12 GM) and 24 cord ROIs (12 WM and 12 GM). As in (Schober et al., 2018), we interpreted r less than 0.4 as weak correlation, r between 0.4 and 0.69 as moderate correlation, r between 0.70 and 0.89 as strong correlation, and r greater than 0.90 as very strong correlation.

TRV was compute across the 24 ROIs (for both brain and cord) for each parameter θ as:

$$TRV = \frac{\sqrt{\pi}}{2N} \sum_{i=1}^{N} \frac{|\Delta_\theta(x_i)|}{\mu_\theta(x_i)}$$

where $\Delta_\theta(x_i)$ and $\mu_\theta(x_i)$ were the difference and average of the test and retest estimates of the parameter θ in the ith ROI x_i.

Finally, ICC was calculated using a two-way mixed effects, single measurement model, using the Matlab ICC function available through Mathworks File Exchange (Salarian, 2024). As in (Schiavi et al., 2022; Veraart et al., 2021), we interpreted ICC less than 0.5 as poor reliability, ICC between 0.5 and 0.75 as moderate reliability, ICC between 0.75 and 0.9 as good reliability, and ICC greater than 0.9 as excellent reliability.

Finally, to assess variation across the brain and cord, we plot the distributions of parameters, for each model, across the 12 WM and 12 GM regions of interest. To statistically determine if the mean values of each derived metric differed significantly across these anatomical regions, a separate one-way repeated measures Analysis of Variance (RM-ANOVA) was performed for each metric within each tissue type (WM and GM) and structure (brain and cord). The within-subjects factor for these ANOVAs were the regions of interest. Prior to interpreting the ANOVA results, Mauchly's test was used to assess the assumption of sphericity. If sphericity was violated (p < 0.05), the Greenhouse-Geisser correction was applied to the degrees of freedom. A significant RM-ANOVA (p < 0.05) indicated that the mean of the metric was not consistent across all anatomical regions examined.

Results

Acquisition is feasible, resulting in high image quality, even at high b-values

Figure 3 shows example diffusion weighted images in the brain and cord for 5 randomly selected subjects, at all b-values. In the brain, contrast is observed across white matter regions with varying orientations, with high signal in pathways orthogonal to the diffusion sensitization directions, even at b=6000. In the cord, contrast is observed across white and gray matter tissue, with the gray matter 'butterfly' visible at lower diffusion-weighted signal indicative of less restrictions and greater diffusivity. However, there is significant partial volume between the tissues due the small size of the intra-cord structures. Regardless, signal remains when diffusion sensitization is orthogonal to the cord, even at b=6000. **Table 1** reports the apparent SNR in the cord for all subjects and rescans. In line with existing literature in the brain, our apparent SNR in WM and GM of 42.8 and 42.8, respectively. The SNR of the cord was lower, with an average value in WM and GM of 16.5 and 24.0, respectively, in line with the lower voxel sizes acquired in the cord.

DTI and multi-compartment models show reasonable contrast between and within tissues

Figure 4 shows DTI parameter maps for 5 subjects. In the brain, white and gray matter contrast is visible in all maps, with values typical of that in the literature (Alexander et al., 2007; Kim et al., 2025; Pierpaoli et al., 1996; Song et al., 2002). In the cord, white and gray matter contrast is most visible in FA and AD maps, although partial volume effects are apparent. White matter cord values of FA, MD are qualitatively similar to that of the brain, although AD appears to be greater in the cord.

Figure 5 shows SMI parameter maps for 5 subjects. Again, in agreement with the literature, not only is there white matter/gray matter contrast, but variation across white matter, particularly within neurite fraction (f) and orientation dispersion (p_2). Freewater fraction (f_w) is 0 or near-0 in white matter. **Figure 5** displays the first SMI-derived maps of the spinal cord. Here, some contrast is noticeable between tissues, with gray matter visually having reduced neurite fraction (f) and $D_e^\perp$, although the full gray matter butterfly is not clearly delineated. The freewater fraction is non-negligible throughout the cord, particularly on voxels neighboring the CSF, but also throughout the entire tissue, further suggesting partial volume effects in the cord.

Figure 6 shows SANDI model parameters for 5 subjects. Neurite fraction and diffusivities in the white matter of the brain well-match those of the simpler SMI model. Unique from SMI, we now have soma fraction and soma radii, both of which are increased in gray matter, with some variation across lobes. SANDI in the cord suggests less visible contrast between tissue types, particularly with soma size and fraction, although the cord-averaged value appears to be in line with that of the brain white matter. Some intra-cord contrast is visible with D_e and $f_{neurite}$ parameters, although again, partial volume effects are clear, and the GM shape is not clearly delineated. All descriptors of neurites and soma are relatively homogenous across the cord, and qualitatively similar to the values in WM of the brain.

DTI is highly reproducible in the brain, SMI and SANDI reproducibility is comparable to that of DTI

To assess reproducibility of the microstructural measures in the brain provided by SMI and SANDI, we compared test-retest reproducibility with those obtained from DTI (the gold standard in clinical practice) as done in (Schiavi et al., 2022). This is shown as scatter plots and Pearson correlation coefficient r shown in **Figure 7**. Pearson r measures range from 0.63-0.98 for DTI-derived measures, with the highest for FA, describing orientation coherence. Both SMI and SANDI have similar reproducibility, with Pearson r ranging from 0.62-0.96 (with the exception of $D_e^\perp$), and 0.45-0.98, respectively. For both, neurite fractions are highly reproducible, as are orientation dispersion (p_2) from SMI and soma fraction (f_{soma}) from SANDI, with the lowest reproducibility associated with extracellular diffusivities.

DTI is moderately reproducible in the cord, SMI and SANDI reproducibility less than that of DTI

Similarly, reproducibility of diffusion measures in the cord are assessed using test-retest scans and are shown in scatter plots in **Figure 8**. Overall, reproducibility is reduced but remains moderate for most measures. DTI ranges from 0.33-0.75 with lowest reproducibility of MD, SMI ranges from 0.33-0.77 with lowest also for extracellular diffusivity measures, and SANDI from 0.12-0.64, with low reproducibility for intracellular diffusivity (D_{in}) and f_{soma}.

Measures show low test-retest variability, moderate ICC
TRV and ICC for DTI, SMI, and SANDI models, in the brain and cord, are shown in **Table 2**. Test-retest variability of SANDI and SMI is on par with that of DTI. TRV ranges of DTI, SMI, and SANDI in the cord are 7.5-11.3, 3.4-31.1, and 3.9-12.0 while those in the brain are 5.2-13.1, 3.6-28.2, and 2.0-19.69. Thus, while Pearson r across regions is low, the metrics themselves show little deviation between scan and rescan, and similar values in the spinal cord as in the brain. In general, ICC decreases from DTI, to SMI, to SANDI, and decreases from brain to cord (although this is not true across all measures), with particularly low reliability (low ICC) of D_{in} and f_{soma} in the cord.

Soma and Neurite Density and organization show contrast within and between tissue types in the brain
Figure 9 shows distributions across the sample population of microstructural measures across the brain, for both WM (Figure 9, left) and GM (Figure 9, right) regions. For all models, several measures show clear trends across white and gray matter regions. For example, DTI measures of FA and AD, SMI measures of f, $D_e^{\parallel}$, and p_2, and SANDI measures of $f_{neurite}$, f_{extra}, and f_{soma} show clear variation across white matter (while many others also reach statistical significance). These same metrics additionally show trends across gray matter regions, with SANDI offering additional soma-based contrast that varies across the cortex. In all cases, measures are more similar to contralateral regions than across regions of the same hemisphere.

Soma and Neurite Density and organization show contrast within tissue types in the cord
Figure 10 shows regional values of DTI, SMT, and SANDI-derived microstructural measures across the cord, for both WM (Figure 10, left), and GM (Figure 10, Right). As in the brain, all models show regional heterogeneity in both tissue types, although with less visible contrast than that in the brain. For example, DTI (AD, MD), and SMI (D_a, f, $D_e^{\perp}$, f_w), show contrast across white matter pathways (with none reaching statistical significance in WM for SANDI), while most measures show contrast across gray matter regions. All SMI measures show clear gray matter trends, and the soma-based SANDI measures also show differences **across** the ventral horn, intermediate zone, and dorsal horns. Again, measures are more similar to contralateral regions than across regions of the same hemisphere.

Discussion
We implemented a clinically feasible diffusion protocol for the in vivo human brain and spinal cord that enables modeling of the white and gray matter tissue microstructure

of a large portion of the central nervous system. Specifically, this protocol enables DTI, the standard model of white matter (SMI), and its extension to gray matter via the SANDI model. We show that derived microstructural measures exhibit reasonable and expected tissue contrast in the brain and cord, with contrast across and within both white and gray matter of both structures. Notably, this study also represents the first images of SMI and SANDI modeling of the spinal cord, and the resulting contrasts and values are reasonable and within expectations given knowledge of brain data. However, the partial volume effects and small intra-cord structures provides insight into the current challenges and requirements for improvements to better characterize the entire central nervous system.

Acquisition and considerations

The data acquisition takes approximately 16 minutes for each anatomy (brain and cord), and includes 6 b-values, 176 total diffusion weighted images, and 24 b=0 images. While we implement DTI, SMI, and SANDI, this acquisition also enables commonly employed multicompartment models that require only multiple shells using standard PGSE sequences, for example Neurite Orientation Dispersion and Density Imaging (NODDI) (Zhang et al., 2012), Freewater DTI (Pasternak et al., 2009), Spherical Mean Technique (SMT) (Kaden, Kruggel, et al., 2016), White Matter Tract Imaging (WMTI) (Jelescu et al., 2015), among others.

The protocol was inspired by optimization performed by Schiavi et al. (Schiavi et al., 2022), who optimized a protocol for the human brain for the SANDI model, within the constraints of their 3T scanner equipped with 80mT/m gradients. By generating simulated tissue substrates, they assess bias and reproducibility of various acquisition schemes, ranging from 14 shells down to 6, and showing that at realistic noise levels (SNR = 100 after spherical averaging over all directions) reducing from 14 to 6 shells has no major impact on parameter estimation. However, a major challenge to acquisition on these systems is the long diffusion times, $\delta =24$ ms and $\Delta =51$ ms, which lead to an increased TE (and decreased SNR) but also an increased sensitivity to exchange, which may violate assumptions of the model and bias parameter estimation. Optimistically, with exchange between compartments on the scale of ~20-50ms (as estimated in rat brain cortex (Jelescu et al., 2022)), biases due to exchange are lower than the impact of noise, however, biases still range on the order of 5-15% for most parameters. Similarly, the authors (Schiavi et al., 2022), and others (Dhital et al., 2019; Howard et al., 2022), highlight that measures such as D_{in} are neither accurate nor precise without alternative acquisitions (linear and planar encodings, or varying diffusion times (Coelho et al., 2019)), which matches our results where D_{in} has lowest scan-rescan reproducibility in both the brain and cord.

While the protocol matched that of Schiavi et al. (Schiavi et al., 2022) in the brain, several innovations were needed in the spinal cord. Typical spinal cord diffusion protocols suggest cardiac triggering during the same point in the cardiac cycle to minimize susceptibility to motion effects (Cohen-Adad et al., 2021), however, this reduces scan efficiency and would result in tremendously long scan times to acquire ~200 total image volumes. Recent work (Kurt et al., 2023) suggests that removing cardiac triggering, which enables acquiring ~60% more data, combined with denoising, motion correction, and outlier removal and replacement, results in measures of similar DTI indices, with similar

reproducibility as triggered acquisitions. In this work, we removed triggering (which also enables harmonization between brain and cord by keeping TR similar), applied MPPCA denoising (Veraart, Novikov, et al., 2016), used spinal cord-specific motion correction (Xu et al., 2013) with slice-wise regularization along the cord and grouping of 8 successive low SNR volumes to improve robustness, and finally implemented a Patch2Self denoising algorithm that replaces outlier signals (i.e. slice dropouts) (Fadnavis et al., 2020; Pizzolato et al., 2023; Kurt G. Schilling et al., 2021). We note that we did not apply distortion correction, as these algorithms have not been fully optimized in the cord and do not quantitatively nor qualitatively improve derived metrics (Schilling et al., 2024; Snoussi et al., 2019; Snoussi et al., 2021). Overall, the acquisition and subsequent preprocessing resulted in high-fidelity images with white and gray matter contrast in diffusion weighted images, and facilitated DTI, SMI, and SANDI-based modeling on a clinical scanner.

Brain and Cord

A major innovation in this work is the feasibility of a harmonized acquisition that will enable characterization and quantification of diffusion-based measures of soma and neurite densities and organizations, and possible biomarkers, throughout the neuroaxis from brain to cervical cord. Most studies of the central nervous system study the brain or cord in isolation, whereas both structures may contribute to clinical deficits. We hypothesize that the ability to simultaneously examine both will advance our understanding of various central nervous system pathologies.

One such example is multiple sclerosis (MS). Conventional MRI facilitates lesion visualization and quantification, in both brain and cord, yet lacks specificity to axonal content, both within lesions and in normal appearing tissue. Because of this, conventional T1 or T2 weighted measures of lesion load in the brain or in the cord only reveal low to moderate associations with cognitive or motor functions (Hackmack et al., 2012; Johnen et al., 2019; Mollison et al., 2017). Utilizing advanced diffusion MRI to provide measures of neurite and soma organization, size, and density, and subsequent neurite/soma loss, swelling/shrinking, or edema may enable higher sensitivity to functional changes with the increased specificity to tissue microstructural changes. Recent changes to the McDonald criteria for MS diagnosis (in 2017 and 2024) included dissemination of lesions in space by including both brain and spinal cord lesions (in structural images), with the goal of moving towards a biological diagnosis (as opposed to clinical means/symptoms); expanding the arsenal of tools to query tissue microstructure is a prerequisite to provide a more comprehensive picture of the disease.

Our results show some consistency between these two structures connected by the ascending and descending projection pathways. Using our protocol, the white matter of the cord exhibits anisotropies (FA, p_2) within the range expected of white matter in the brain. Similar results are observed for diffusivities, both axonal and extra-axonal, as well as neurite fractions. Future work may investigate a pathway-specific analysis of the decussating and non-decussating corticospinal tracts to assess the feasibility of studying the length of this pathway from the cortex to the cord. Overall, our results show reasonable contrast from the brain to the cord, with values within expected ranges (despite differences in SNR and resolution) for white and gray matter microstructures.

Multicompartment modeling of the spinal cord

This is the first application of the SMI and SANDI models in the in vivo human spinal cord. Previous works have characterized white and gray matter in the cord using NODDI and SMT, providing evidence of dispersion and neurite density changes in disease (MS) in both lesion and normal appearing tissue, as well as providing normative values metrics in the healthy cord(By et al., 2017, 2018; Grussu et al., 2017; Grussu et al., 2015; Kurt G Schilling et al., 2021). Here, we show that SMI and SANDI similarly provide contrast among the various white matter pathways and gray matter regions where heterogenous axonal environments are expected.

The advantage of SMI is that it encompasses a number of WM models made to capture Gaussian compartments, with axons represented by sticks (Coelho et al., 2022). While other models impose constraints on parameters, between parameters, or on forms of the fiber distribution to improve robustness, they may introduce biases into the parameter estimation. Here, supervised machine learning is used to improve precision of parameter estimates (Coelho et al., 2022), while also providing microstructural maps without constraints or priors. We find neurite fractions of ~.4-.5, axial diffusivity >2 (and greater than extra-axonal parallel diffusivity), orientation dispersion (p_2) ~0.7, and a relatively large partial volume fraction with free water (~.15-.2). These maps are all in line with that observed in the brain white matter (Coelho et al., 2022) (although with larger partial volume fraction with free water, and subsequently smaller neurite fraction), with maps that are anatomically and microstructurally feasible.

The advantage of the SANDI model is explicit modeling of compartments that are prevalent in the gray matter, in particular soma size and soma fraction (Palombo et al., 2020). This necessitates the high b-value data, for increased sensitivity to the small, restricted spherical compartments. Here, the disadvantage is the increased TE to reach this diffusion weighting, decreasing signal and increasing diffusion times. SMI, above, may benefit from a multi-shell acquisition that is limited to a b-value of ~2000-3000 instead of occurring the signal loss associated with also modeling SANDI. The increased diffusion times increase biases due to exchange, for which there is no consensus on the time scale in the cord, and limits sensitivity to smaller soma. Despite this, this model also results in an intracellular diffusivity slightly greater than extracellular parallel diffusivity, and a neurite fraction of ~.3-.45.

On the optimistic side, both models result in quantitative differences across both white and gray matter tissues, which is expected in the cord. For example, differences in locations of sensory synapses (dorsal horn) and motor cell bodies (ventral horn), along with branching nerve roots are expected to result in different microstructural environments across these structures. Moreover, reproducibility (particularly TRV) of most measures derived from SMI/SANDI was similar to that of DTI, with generally similar values between brain and cord. However, ICC was (in general) lower in the cord than brain. Some of this can be attributed smaller voxel volume in the cord, smaller tissues of interest and potentially incompletely mitigated motion.

Similarly, for white and gray matter contrast, partial volume effects from the small size and incompletely mitigated motion (across volumes), geometric distortion, and atlas-based tissue segmentation play a role. Together, this makes localization of specific changes in the small (often less than the size of a voxel) ascending/descending pathways or gray matter horns challenging, losing some of the spatial specificity but gaining mictostructural specificity gained with multi-compartment modeling. Another challenge is the large axons of the spinal cord, with a volume-weighted mean axon diameter often on the order of 2-5um depending on pathway, which may violate assumptions of a zero-radius cylinder (i.e., a stick) for the neurite compartment. Veraart et al. (Veraart et al., 2019; Veraart et al., 2020), show that in vivo human brain, this assumption holds valid when using clinical scanners and subsequently long diffusion times, with the neurites indistinguishable from sticks. Similar studies should be performed in the cord to assess sensitivity to non-negligible axon radii.

Limitations and Future

There are several limitations that must be acknowledged. First, is the limited sample size (N=11) of the current study. While 11 subjects (and N=5 rescans) is sufficient to assess reproducibility (Koller et al., 2021; Schiavi et al., 2022; Veraart et al., 2021), it is not sufficient to provide comprehensive normative values across the population, nor is this a validation of the derived indices. However, the goal was to demonstrate the potential of capturing newly-developed contrasts within and across tissue types on a clinical scanner. Second, these models may not be suitable for this acquisition – with these noise properties, diffusion times, and PGSE acquisition. For gray matter in particular, the long diffusion times increase susceptibility to water exchange biases. While reported exchange times vary (Jelescu & Novikov, 2020; Novikov, 2021), some estimates (often from *ex vivo* studies) are as fast as ~10 ms (Olesen et al., 2022; Williamson et al., 2019), much shorter than our acquired diffusion times. As these models do not account for time dependence, their accuracy in GM is limited should such fast exchange occur *in vivo*. In addition to biases described above due to long diffusion times, variance due to noise in parameter estimation, and possibly invalid stick-like assumptions in neurites, the use of alternative diffusion weightings (planar, spherical) may better condition model-fitting (Coelho et al., 2022), and should be investigated in the future.

Next, while a ~16 acquisition time per anatomical structure is comparable to advanced research protocols, the total duration for comprehensive brain and cord imaging, combined with 80mT/m gradient systems and multi-stage processing, may limit widespread clinical adoption. Further research is necessary to validate the specific clinical utilized of the derived SMI or SANDI metrics for various neurological conditions. Improvements in spinal cord image processing are also needed, including optimizing preprocessing associated with high b-value data, which challenges distortion and motion correction when most volumes are expected to be at the noise level. Finally, future studies should investigate the clinical utility of combining brain and cord features in studying neurological disorders, and use similar acquisitions to investigate the relationship between brain and cord.

Conclusion

We have presented and evaluated a harmonized diffusion protocol to study the brain and spinal cord on a clinical scanner. The protocol enables DTI modeling, as well as advanced SMI and SANDI models to improve specificity in characterizing neurite and soma organization. We demonstrate feasibility of acquiring multi-shell diffusion data at high b-values and high SNR, show qualitatively reasonable contrast across brain and cord, and show SMI and SANDI have moderate reproducibility relative to DTI, with higher scan rescan variability in the cord than in the brain. Finally, we demonstrate that soma and neurite density with these models shows contrast across white matter pathways, and across gray matter regions in both structures, which is expected given known variation in neurite densities and diameters and cellular architectures and densities. This protocol can be employed in a reasonable amount of time to study CNS pathologies and investigate biomarkers of structural integrity throughout the neuroaxis.

Author Contributions

KGS (writing, analysis, conceptualization); MP (analysis, experimental design); AAW (experimental design, data curation); KPOG (experimental design, data curation); MP (experimental design, analysis); BAL (funding, conceptualization, supervision); SAS (funding, conceptualization, supervision)
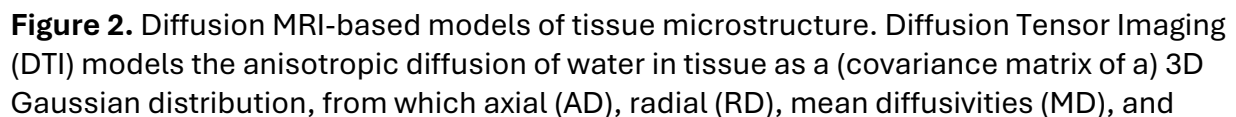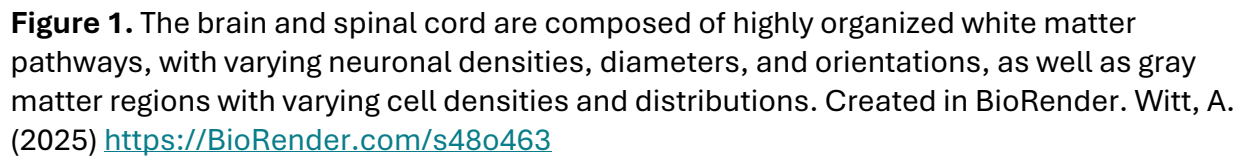
Declaration of competing interest

The authors have no competing interests to declare.

Ethics

All participants from whom data were used in this manuscript, provided written informed consent (and consent to publish) according to the declaration of Helsinki.

Data and Code Availability

Data available in BIDS format in Zenodo sharing platform (https://doi.org/10.5281/zenodo.15512428) (doi: 10.5281/zenodo.15512428).

Figure 1. The brain and spinal cord are composed of highly organized white matter pathways, with varying neuronal densities, diameters, and orientations, as well as gray matter regions with varying cell densities and distributions. Created in BioRender. Witt, A. (2025) https://BioRender.com/s48o463

Figure 2. Diffusion MRI-based models of tissue microstructure. Diffusion Tensor Imaging (DTI) models the anisotropic diffusion of water in tissue as a (covariance matrix of a) 3D Gaussian distribution, from which axial (AD), radial (RD), mean diffusivities (MD), and

fractional anisotropy (FA) can be derived. Standard Model Imaging (SMI) represents tissue as zero-radius sticks embedded within an extra-axonal space described – and results in indices of axonal fraction (f), along-axon diffusivity (D_a), extra-axonal parallel ($D_e^{\parallel}$) and perpendicular ($D_e^{\perp}$) diffusivities, free water (signal) fraction (fw), and a measure of fiber dispersion (p_2). Soma And Neurite Density Imaging (SANDI) models water diffusion within neurites (stick-like axons and dendrites) and soma (spherical neuronal cell bodies), extending the standard model to also include soma fraction (f_{soma}) and soma radii (R_{soma}).

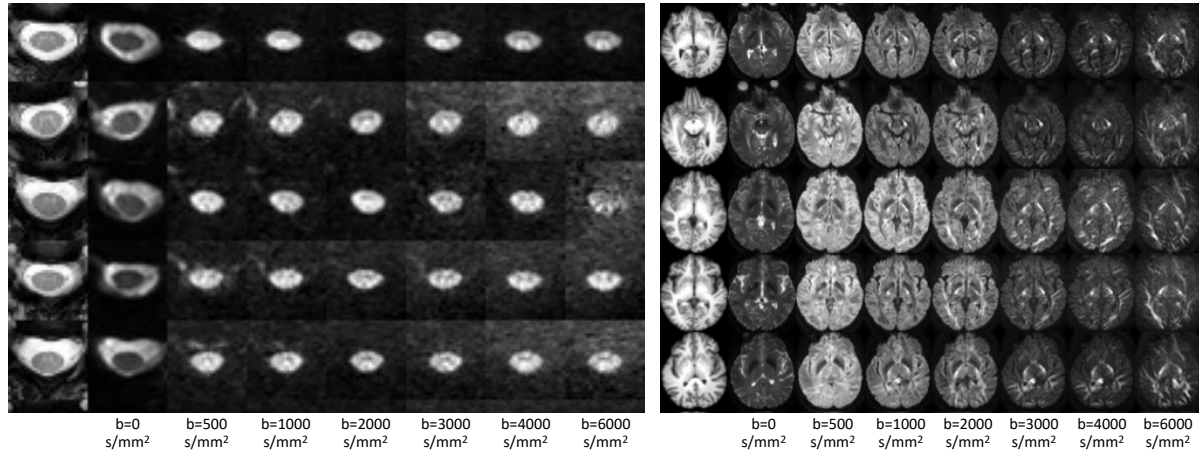| b=0 s/mm² | b=500 s/mm² | b=1000 s/mm² | b=2000 s/mm² | b=3000 s/mm² | b=4000 s/mm² | b=6000 s/mm² | b=0 s/mm² | b=500 s/mm² | b=1000 s/mm² | b=2000 s/mm² | b=3000 s/mm² | b=4000 s/mm² | b=6000 s/mm² |

Figure 3. Data acquisition is feasible on a clinical scanner in the brain and spinal cord. A representative axial slice of 5 subjects is shown for the brain and cord, along with a diffusion weighted image sensitized along the Left/Right direction at b-values ranging from 0 to 6000 s/mm². Contrast is visible within and across tissue types.

Subject	Cord			Brain		
	WM	**GM**	**WM+GM**	**WM**	**GM**	**WM+GM**
S001	11.8	19.3	12.5	42.1	47.4	43.0
S002	25.0	34.9	26.0	36.2	39.9	36.1
S002-rescan	16.1	22.9	16.9	48.6	48.9	46.5
S003	11.9	18.9	12.5	44.6	48.6	44.8
S004	11.7	17.5	12.3	60.6	60.0	57.2
S005	10.9	14.0	11.2	56.7	59.7	55.8
S005-rescan	19.6	28.4	20.5	36.3	34.7	33.6
S006	25.0	35.6	26.1	NaN	NaN	NaN
S006-rescan	15.5	20.9	16.1	47.9	49.2	46.8
S007	9.8	13.9	10.3	41.6	38.2	38.0
S007-rescan	13.5	18.3	14.1	42.2	39.2	39.1
S008	16.5	26.8	17.4	44.6	41.7	41.7
S008-rescan	28.3	36.8	29.3	30.7	35.2	32.2
S009	16.8	29.5	17.8	43.7	45.9	43.0
S009-rescan	11.9	18.5	12.5	37.3	34.3	33.7
S010	18.8	25.3	19.4	45.4	41.3	41.4
S011	17.4	27.2	18.2	25.7	21.3	21.5

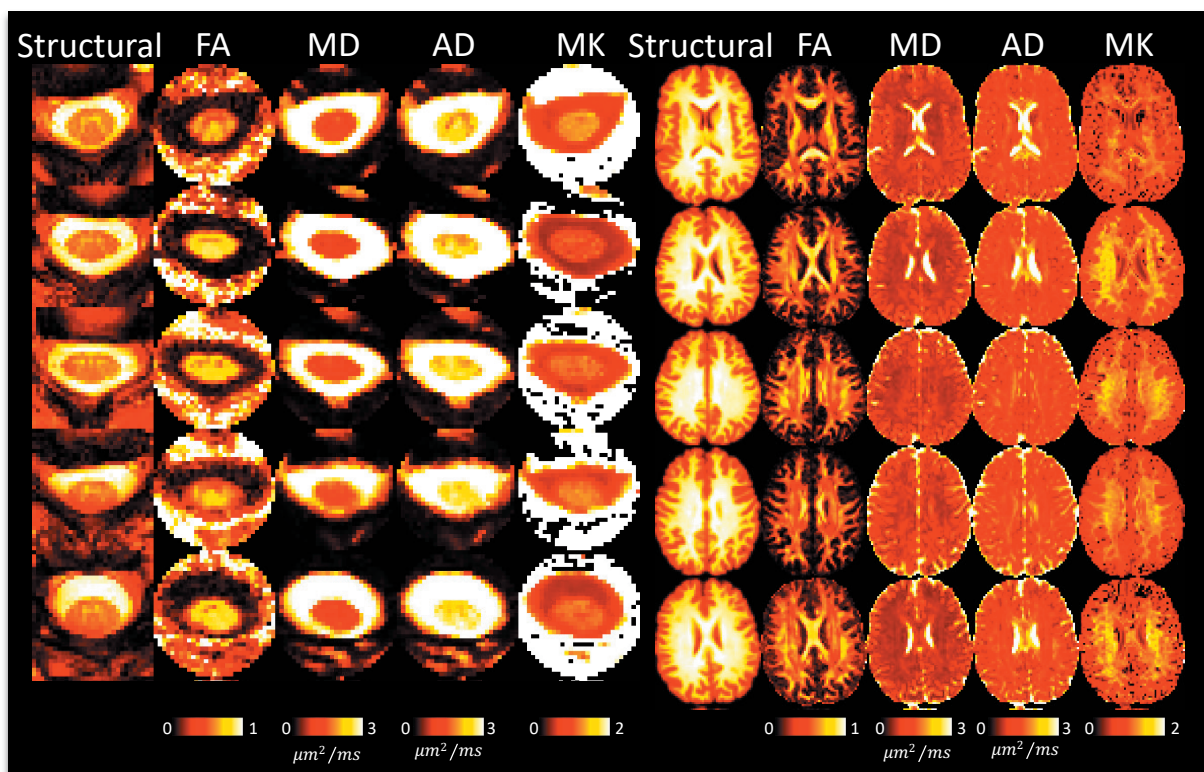**Table 1.** Apparent SNR for WM and GM in the brain and cord.

Figure 4. DTI shows reasonable contrast between and within tissues in the brain and spinal cord. A representative axial slice of 5 randomly-selected subjects (5 rows) is shown for the brain and cord, showing the structural image and the corresponding DTI-based contrasts.
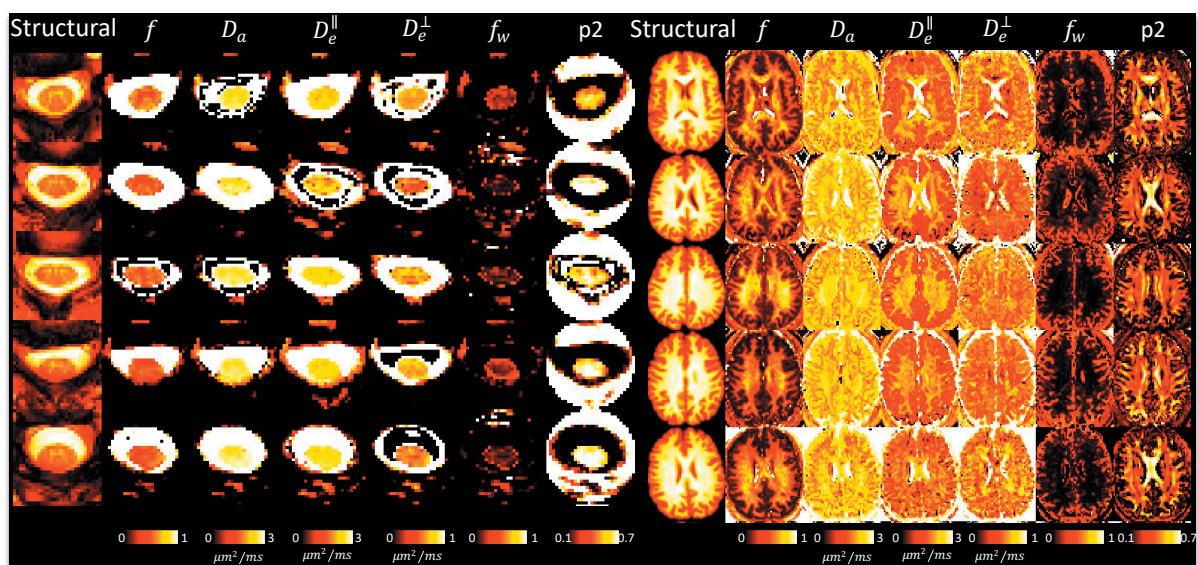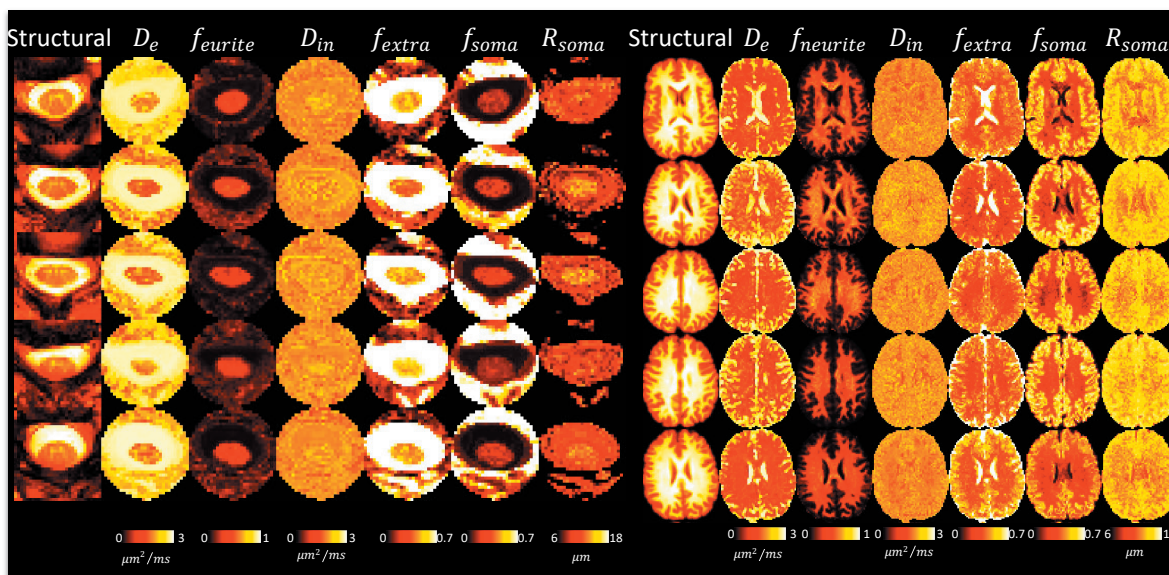
Figure 5. SMI shows reasonable contrast between and within tissues in the brain and spinal cord. A representative axial slice of 5 randomly-selected subjects (5 rows) is shown for the brain and cord, showing the structural image and the corresponding SMI-based contrasts.

Figure 6. SANDI shows reasonable contrast between and within tissues in the brain and spinal cord. A representative axial slice of 5 randomly-selected subjects (5 rows) is shown for the brain and cord, showing the structural image and the corresponding SMI-based contrasts.
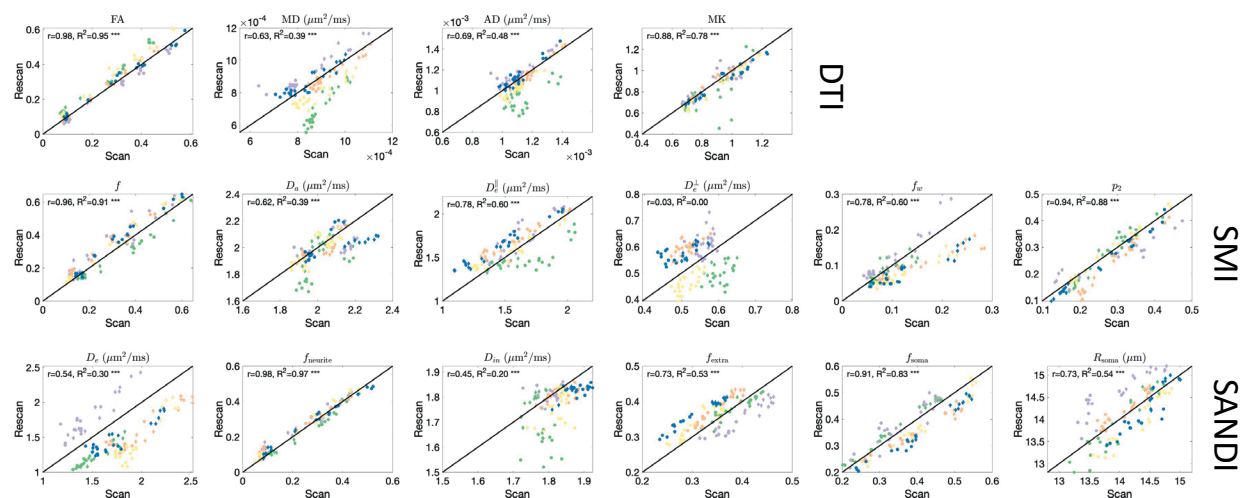
Figure 7. Repeatability of microstructural measures in the brain. Scatter plots of scan-rescan microstructural measures extract from 12GM and 12WM regions are shown for DTI, SMI, and SANDI models. Points are colored based on subjects.
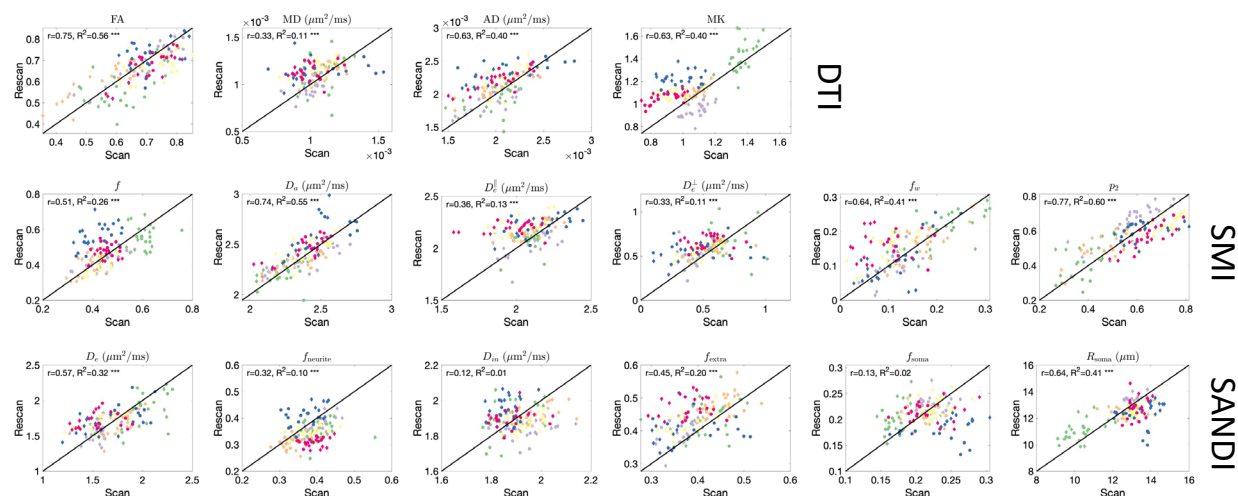

Figure 8. Repeatability of microstructural measures in the cord. Scatter plots of scan-rescan microstructural measures extract from 12GM and 12WM regions are shown for DTI, SMI, and SANDI models. Points are colored based on subjects.

	SPINAL CORD						BRAIN					
	DTI						**DTI**					
	FA	MD	AD	MK			FA	MD	AD	MK		
	8.02	10.75	7.57	11.33			13.31	9.12	6.82	5.25		
	SMI						**SMI**					
TRV	f	Da	De_par	De_perp	fw	p2	f	D_a	De_par	De_perp	fw	p2
	11.89	3.42	5.30	22.65	31.08	11.41	14.32	3.63	7.60	12.17	28.19	11.43
	SANDI						**SANDI**					
	De	fneurite	Din	fextra	fsoma	Rsoma	De	fneurite	Din	fextra	fsoma	Rsoma
	8.72	11.94	3.91	11.42	11.99	5.54	19.69	12.19	2.66	8.55	9.17	1.99
	DTI						**DTI**					
	FA	MD	AD	MK			FA	MD	AD	MK		
	0.74	0.29	0.60	0.56			0.97	0.57	0.63	0.87		
	SMI						**SMI**					
ICC	f	Da	De_par	De_perp	fw	p2	f	Da	De_par	De_perp	fw	p2
	0.50	0.74	0.30	0.29	0.62	0.76	0.95	0.56	0.75	0.03	0.68	0.92
	SANDI						**SANDI**					
	De	fneurite	Din	fextra	fsoma	Rsoma	De	fneurite	Din	fextra	fsoma	Rsoma
	0.54	0.25	0.12	0.35	0.12	0.59	0.43	0.98	0.34	0.69	0.89	0.71

Table 2. Reproducibility and Intraclass Correlation Coefficient of microstructural measures in the brain and cord.
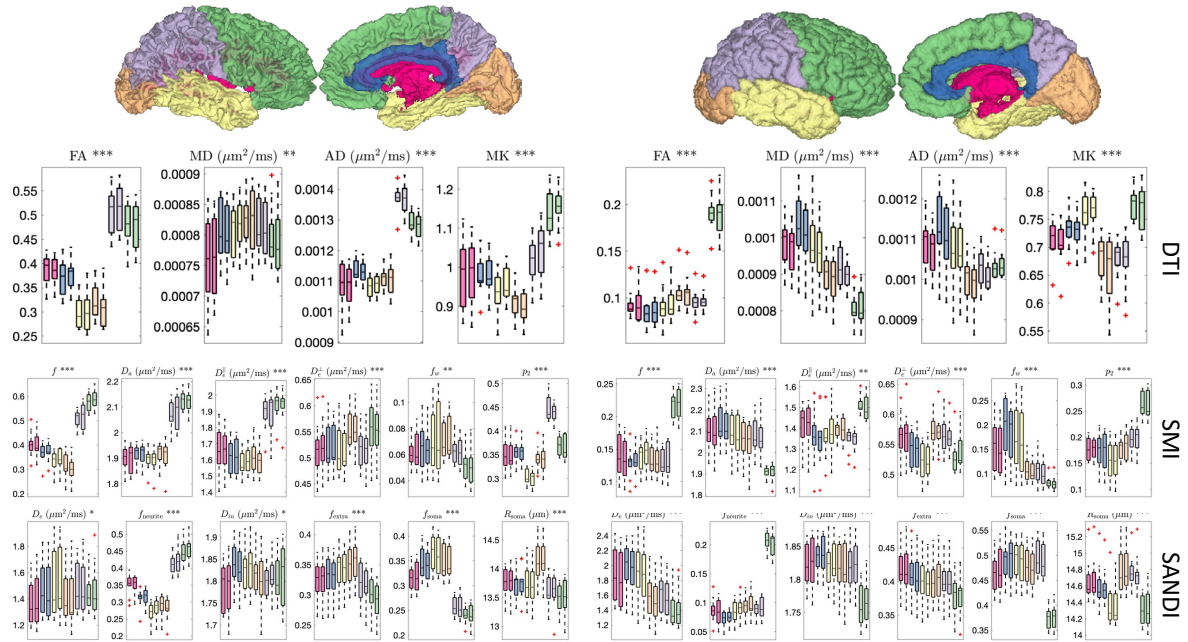
Figure 9. DTI (top), SMI (middle), and SANDI (bottom) show contrast between and within white matter regions (left) and gray matter regions (right). Plots are colored based on location in the lobes of the brain and corresponding white matter regions. For each metric, asterisks in the plot title indicate the level of overall statistical significance for differences across regions, as determined by a one-way repeated measures ANOVA (*p < 0.05, **p < 0.01, ***p < 0.001).
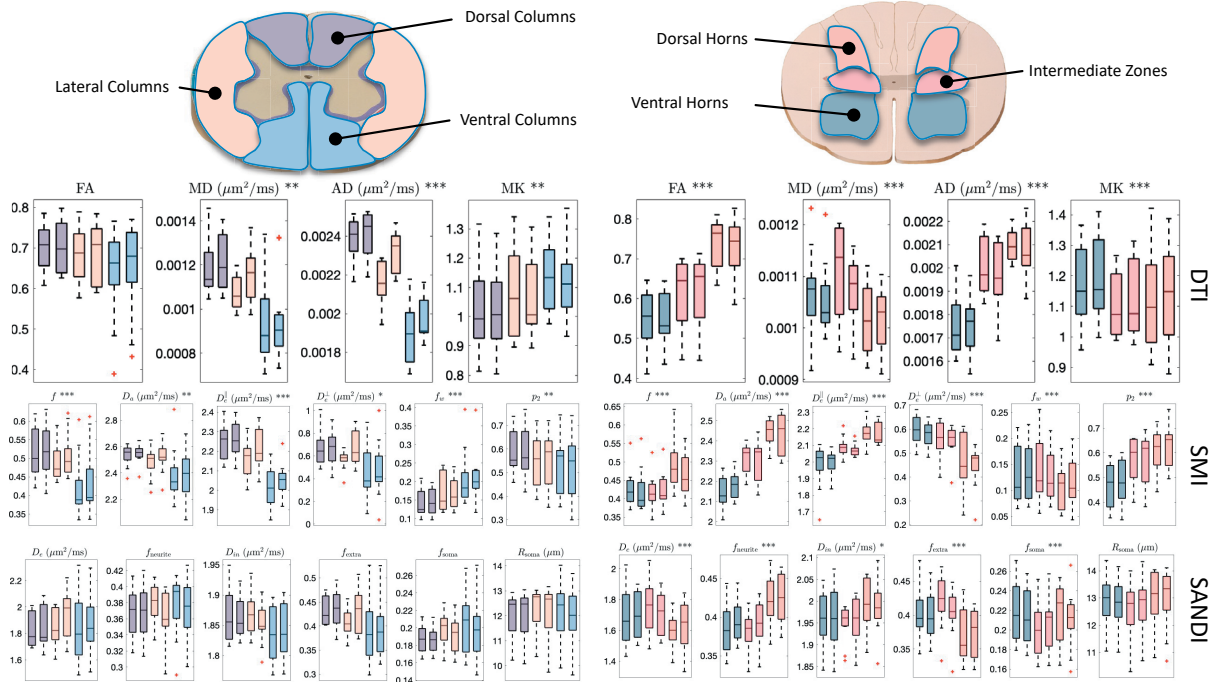
Figure 10. DTI (top), SMI (middle), and SANDI (bottom) show contrast within and between the somatotopically organized white and gray matter regions. Plots are colored based on location in the white matter (bilateral Dorsal Columns, Lateral Funiculi, Ventral Funiculi) and gray matter (dorsal horn, intermediate zone, and ventral horns). For each metric, asterisks in the plot title indicate the level of overall statistical significance for differences across regions, as determined by a one-way repeated measures ANOVA (*p < 0.05, **p < 0.01, ***p < 0.001).

References

Alexander, A. L., Lee, J. E., Lazar, M., & Field, A. S. (2007). Diffusion tensor imaging of the brain. *Neurotherapeutics*, *4*(3), 316-329. https://doi.org/10.1016/j.nurt.2007.05.011

Andersson, J. L., Skare, S., & Ashburner, J. (2003). How to correct susceptibility distortions in spin-echo echo-planar images: application to diffusion tensor imaging. *Neuroimage*, *20*(2), 870-888. https://doi.org/10.1016/S1053-8119(03)00336-7

Andersson, J. L. R., Graham, M. S., Zsoldos, E., & Sotiropoulos, S. N. (2016). Incorporating outlier detection and replacement into a non-parametric framework for movement and distortion correction of diffusion MR images. *Neuroimage*, *141*, 556-572. https://doi.org/10.1016/j.neuroimage.2016.06.058

Basser, P. J., Mattiello, J., & LeBihan, D. (1994). MR diffusion tensor spectroscopy and imaging. *Biophys J, 66*(1), 259-267. https://doi.org/10.1016/S0006-3495(94)80775-1

Beaulieu, C. (2002). The basis of anisotropic water diffusion in the nervous system - a technical review. *NMR Biomed, 15*(7-8), 435-455. https://doi.org/10.1002/nbm.782

By, S., Xu, J., Box, B. A., Bagnato, F. R., & Smith, S. A. (2017). Application and evaluation of NODDI in the cervical spinal cord of multiple sclerosis patients. *Neuroimage Clin*, *15*, 333-342. https://doi.org/10.1016/j.nicl.2017.05.010

By, S., Xu, J., Box, B. A., Bagnato, F. R., & Smith, S. A. (2018). Multi-compartmental diffusion characterization of the human cervical spinal cord in vivo using the spherical mean technique. *NMR Biomed*, *31*(4), e3894. https://doi.org/10.1002/nbm.3894

Coelho, S., Baete, S. H., Lemberskiy, G., Ades-Aron, B., Barrol, G., Veraart, J., Novikov, D. S., & Fieremans, E. (2022). Reproducibility of the Standard Model of diffusion in white matter on clinical MRI systems. *Neuroimage*, *257*, 119290. https://doi.org/10.1016/j.neuroimage.2022.119290

Coelho, S., Pozo, J. M., Jespersen, S. N., Jones, D. K., & Frangi, A. F. (2019). Resolving degeneracy in diffusion MRI biophysical model parameter estimation using double diffusion encoding. *Magn Reson Med*, *82*(1), 395-410. https://doi.org/10.1002/mrm.27714

Cohen-Adad, J., Alonso-Ortiz, E., Abramovic, M., Arneitz, C., Atcheson, N., Barlow, L., Barry, R. L., Barth, M., Battiston, M., Buchel, C., Budde, M., Callot, V., Combes, A. J. E., De Leener, B., Descoteaux, M., de Sousa, P. L., Dostal, M., Doyon, J., Dvorak, A.,...Xu, J. (2021). Generic acquisition protocol for quantitative MRI of the spinal cord. *Nat Protoc*. https://doi.org/10.1038/s41596-021-00588-0

Coronado-Leija, R., Abdollahzadeh, A., Lee, H. H., Coelho, S., Ades-Aron, B., Liao, Y., Salo, R. A., Tohka, J., Sierra, A., Novikov, D. S., & Fieremans, E. (2024). Volume electron microscopy in injured rat brain validates white matter microstructure metrics from diffusion MRI. *ArXiv*. https://www.ncbi.nlm.nih.gov/pubmed/38259346

De Leener, B., Fonov, V. S., Collins, D. L., Callot, V., Stikov, N., & Cohen-Adad, J. (2018). PAM50: Unbiased multimodal template of the brainstem and spinal cord aligned with the ICBM152 space. *Neuroimage*, *165*, 170-179. https://doi.org/10.1016/j.neuroimage.2017.10.041

De Leener, B., Lévy, S., Dupont, S. M., Fonov, V. S., Stikov, N., Louis Collins, D., Callot, V., & Cohen-Adad, J. (2017). SCT: Spinal Cord Toolbox, an open-source software for processing spinal cord MRI data. *Neuroimage*, *145*(Pt A), 24-43. https://doi.org/10.1016/j.neuroimage.2016.10.009

Dhital, B., Reisert, M., Kellner, E., & Kiselev, V. G. (2019). Intra-axonal diffusivity in brain white matter. *Neuroimage*, *189*, 543-550. https://doi.org/10.1016/j.neuroimage.2019.01.015

Fadnavis, S., Batson, J., & Garyfallidis, E. (2020). Patch2Self: denoising diffusion MRI with self-supervised learning. *arXiv preprint arXiv:2011.01355*.

Felten, D. (2021). *Netter's atlas of neuroscience* (4. ed.). Elsevier, Inc.

Fieremans, E., Benitez, A., Jensen, J. H., Falangola, M. F., Tabesh, A., Deardorff, R. L., Spampinato, M. V., Babb, J. S., Novikov, D. S., Ferris, S. H., & Helpern, J. A. (2013). Novel white matter tract integrity metrics sensitive to Alzheimer disease progression. *AJNR Am J Neuroradiol*, *34*(11), 2105-2112. https://doi.org/10.3174/ajnr.A3553

Fieremans, E., Jensen, J. H., Helpern, J., Kim, S., Grossman, R. I., Inglese, M., & Novikov, D. (2012). Diffusion distinguishes between axonal loss and demyelination in brain white matter. *Proc. Int. Soc. Magn. Reson. Med.*, *20*.

Fieremans, E., Jensen, J. H., & Helpern, J. A. (2011). White matter characterization with diffusional kurtosis imaging. *Neuroimage*, *58*(1), 177-188. https://doi.org/10.1016/j.neuroimage.2011.06.006

Fischl, B. (2012). FreeSurfer. *Neuroimage*, *62*(2), 774-781. https://doi.org/10.1016/j.neuroimage.2012.01.021

Fischl, B., Salat, D. H., Busa, E., Albert, M., Dieterich, M., Haselgrove, C., van der Kouwe, A., Killiany, R., Kennedy, D., Klaveness, S., Montillo, A., Makris, N., Rosen, B., & Dale, A. M. (2002). Whole brain segmentation: automated labeling of neuroanatomical structures in the human brain. *Neuron*, *33*(3), 341-355. https://doi.org/10.1016/s0896-6273(02)00569-x

Genc, S., Chamberland, M., Koller, K., Tax, C. M. W., Zhang, H., Palombo, M., & Jones, D. K. (2021, 2021//). Repeatability of Soma and Neurite Metrics in Cortical and Subcortical Grey Matter. Computational Diffusion MRI, Cham.

Grussu, F., Schneider, T., Tur, C., Yates, R. L., Tachrount, M., Ianus, A., Yiannakas, M. C., Newcombe, J., Zhang, H., Alexander, D. C., DeLuca, G. C., & Gandini Wheeler-Kingshott, C. A. M. (2017). Neurite dispersion: a new marker of multiple sclerosis spinal cord pathology? *Ann Clin Transl Neurol*, *4*(9), 663-679. https://doi.org/10.1002/acn3.445

Grussu, F., Schneider, T., Zhang, H., Alexander, D. C., & Wheeler-Kingshott, C. A. (2015). Neurite orientation dispersion and density imaging of the healthy cervical spinal cord in vivo. *Neuroimage*, *111*, 590-601. https://doi.org/10.1016/j.neuroimage.2015.01.045

Hackmack, K., Weygandt, M., Wuerfel, J., Pfueller, C. F., Bellmann-Strobl, J., Paul, F., & Haynes, J. D. (2012). Can we overcome the 'clinico-radiological paradox' in multiple sclerosis? *J Neurol*, *259*(10), 2151-2160. https://doi.org/10.1007/s00415-012-6475-9

Held, P., Dorenbeck, U., Seitz, J., Frund, R., & Albrich, H. (2003). MRI of the abnormal cervical spinal cord using 2D spoiled gradient echo multiecho sequence (MEDIC) with magnetization transfer saturation pulse. A T2* weighted feasibility study. *J Neuroradiol*, *30*(2), 83-90. https://www.ncbi.nlm.nih.gov/pubmed/12717293

Howard, A. F., Cottaar, M., Drakesmith, M., Fan, Q., Huang, S. Y., Jones, D. K., Lange, F. J., Mollink, J., Rudrapatna, S. U., Tian, Q., Miller, K. L., & Jbabdi, S. (2022). Estimating axial diffusivity in the NODDI model. *Neuroimage*, *262*, 119535. https://doi.org/10.1016/j.neuroimage.2022.119535

Jelescu, I., & Novikov, D. (2020). Water exchange time between gray matter compartments in vivo. International Society of Magnetic Resonance in Medicine,

Jelescu, I. O., de Skowronski, A., Geffroy, F., Palombo, M., & Novikov, D. S. (2022). Neurite Exchange Imaging (NEXI): A minimal model of diffusion in gray matter with inter-compartment water exchange. *Neuroimage*, *256*, 119277. https://doi.org/10.1016/j.neuroimage.2022.119277

Jelescu, I. O., Veraart, J., Adisetiyo, V., Milla, S. S., Novikov, D. S., & Fieremans, E. (2015). One diffusion acquisition and different white matter models: how does microstructure change in human early development based on WMTI and NODDI? *Neuroimage*, *107*, 242-256. https://doi.org/10.1016/j.neuroimage.2014.12.009

Jelescu, I. O., Veraart, J., Fieremans, E., & Novikov, D. S. (2016). Degeneracy in model parameter estimation for multi-compartmental diffusion in neuronal tissue. *NMR Biomed*, *29*(1), 33-47. https://doi.org/10.1002/nbm.3450

Jelescu, I. O., Zurek, M., Winters, K. V., Veraart, J., Rajaratnam, A., Kim, N. S., Babb, J. S., Shepherd, T. M., Novikov, D. S., Kim, S. G., & Fieremans, E. (2016). In vivo quantification of demyelination and recovery using compartment-specific diffusion MRI metrics validated by electron microscopy. *Neuroimage*, *132*, 104-114. https://doi.org/10.1016/j.neuroimage.2016.02.004

Jenkinson, M., Beckmann, C. F., Behrens, T. E., Woolrich, M. W., & Smith, S. M. (2012). Fsl. *Neuroimage*, *62*(2), 782-790. https://doi.org/10.1016/j.neuroimage.2011.09.015

Jensen, J. H., Helpern, J. A., Ramani, A., Lu, H., & Kaczynski, K. (2005). Diffusional kurtosis imaging: the quantification of non-gaussian water diffusion by means of magnetic resonance imaging. *Magn Reson Med*, *53*(6), 1432-1440. https://doi.org/10.1002/mrm.20508

Jespersen, S. N., Kroenke, C. D., Østergaard, L., Ackerman, J. J., & Yablonskiy, D. A. (2007). Modeling dendrite density from magnetic resonance diffusion measurements. *Neuroimage*, *34*(4), 1473-1486. https://doi.org/10.1016/j.neuroimage.2006.10.037

Johnen, A., Schiffler, P., Landmeyer, N. C., Tenberge, J. G., Riepl, E., Wiendl, H., Kramer, J., & Meuth, S. G. (2019). Resolving the cognitive clinico-radiological paradox - Microstructural degeneration of fronto-striatal-thalamic loops in early active multiple sclerosis. *Cortex*, *121*, 239-252. https://doi.org/10.1016/j.cortex.2019.08.022

Jones, D. K., & Cercignani, M. (2010). Twenty-five pitfalls in the analysis of diffusion MRI data. *NMR Biomed*, *23*(7), 803-820. https://doi.org/10.1002/nbm.1543

Jones, D. K., Horsfield, M. A., & Simmons, A. (1999). Optimal strategies for measuring diffusion in anisotropic systems by magnetic resonance imaging. *Magn Reson Med*, *42*(3), 515-525. https://www.ncbi.nlm.nih.gov/pubmed/10467296

Kaden, E., Kelm, N. D., Carson, R. P., Does, M. D., & Alexander, D. C. (2016). Multi-compartment microscopic diffusion imaging. *Neuroimage*, *139*, 346-359. https://doi.org/10.1016/j.neuroimage.2016.06.002

Kaden, E., Kruggel, F., & Alexander, D. C. (2016). Quantitative mapping of the per-axon diffusion coefficients in brain white matter. *Magn Reson Med*, *75*(4), 1752-1763. https://doi.org/10.1002/mrm.25734

Kellner, E., Dhital, B., Kiselev, V. G., & Reisert, M. (2016). Gibbs-ringing artifact removal based on local subvoxel-shifts. *Magn Reson Med*, *76*(5), 1574-1581. https://doi.org/10.1002/mrm.26054

Kim, M. E., Gao, C., Ramadass, K., Newlin, N. R., Kanakaraj, P., Bogdanov, S., Rudravaram, G., Archer, D., Hohman, T. J., Jefferson, A. L., Morgan, V. L., Roche, A., Englot, D. J., Resnick, S. M., Beason Held, L. L., Cutting, L., Barquero, L. A., D'archangel, M. A., Nguyen, T. Q.,...Schilling, K. G. (2025). White matter microstructure and

macrostructure brain charts across the human lifespan. *bioRxiv*, 2025.2005.2008.652953. https://doi.org/10.1101/2025.05.08.652953

Koller, K., Rudrapatna, U., Chamberland, M., Raven, E. P., Parker, G. D., Tax, C. M. W., Drakesmith, M., Fasano, F., Owen, D., Hughes, G., Charron, C., Evans, C. J., & Jones, D. K. (2021). MICRA: Microstructural image compilation with repeated acquisitions. *Neuroimage*, *225*, 117406. https://doi.org/10.1016/j.neuroimage.2020.117406

Kroenke, C. D., Ackerman, J. J., & Yablonskiy, D. A. (2004). On the nature of the NAA diffusion attenuated MR signal in the central nervous system. *Magn Reson Med*, *52*(5), 1052-1059. https://doi.org/10.1002/mrm.20260

Kurt, G. S., Anna, J. E. C., Karthik, R., Francois, R., Grace, S., Logan, P., Subramaniam, S., Julien, C.-A., John, C. G., Bennett, A. L., Seth, A. S., & Kristin, P. O. G. (2023). Influence of preprocessing, distortion correction and cardiac triggering on the quality of diffusion MR images of spinal cord. *bioRxiv*, 2023.2009.2026.559530. https://doi.org/10.1101/2023.09.26.559530

Le Bihan, D., & Iima, M. (2015). Diffusion Magnetic Resonance Imaging: What Water Tells Us about Biological Tissues. *PLOS Biology*, *13*(7), e1002203. https://doi.org/10.1371/journal.pbio.1002203

Lee, H. H., Papaioannou, A., Kim, S. L., Novikov, D. S., & Fieremans, E. (2020). A time-dependent diffusion MRI signature of axon caliber variations and beading. *Commun Biol*, *3*(1), 354. https://doi.org/10.1038/s42003-020-1050-x

Lévy, S., Benhamou, M., Naaman, C., Rainville, P., Callot, V., & Cohen-Adad, J. (2015). White matter atlas of the human spinal cord with estimation of partial volume effect. *Neuroimage*, *119*, 262-271. https://doi.org/10.1016/j.neuroimage.2015.06.040

Mollison, D., Sellar, R., Bastin, M., Mollison, D., Chandran, S., Wardlaw, J., & Connick, P. (2017). The clinico-radiological paradox of cognitive function and MRI burden of white matter lesions in people with multiple sclerosis: A systematic review and meta-analysis. *PLoS One*, *12*(5), e0177727. https://doi.org/10.1371/journal.pone.0177727

Mori, S., & Zhang, J. (2006). Principles of diffusion tensor imaging and its applications to basic neuroscience research. *Neuron*, *51*(5), 527-539. https://doi.org/10.1016/j.neuron.2006.08.012

Nieuwenhuys, R., Voogd, J., & Huijzen, C. v. (2008). *The human central nervous system* (4th ed.). Springer.

Novikov, D. S. (2021). The present and the future of microstructure MRI: From a paradigm shift to normal science. *J Neurosci Methods*, *351*, 108947. https://doi.org/10.1016/j.jneumeth.2020.108947

Novikov, D. S., Fieremans, E., Jespersen, S. N., & Kiselev, V. G. (2018). Quantifying brain microstructure with diffusion MRI: Theory and parameter estimation. *NMR Biomed*, e3998. https://doi.org/10.1002/nbm.3998

Novikov, D. S., Kiselev, V. G., & Jespersen, S. N. (2018). On modeling. *Magn Reson Med*, *79*(6), 3172-3193. https://doi.org/10.1002/mrm.27101

Novikov, D. S., Veraart, J., Jelescu, I. O., & Fieremans, E. (2018). Rotationally-invariant mapping of scalar and orientational metrics of neuronal microstructure with diffusion MRI. *Neuroimage*, *174*, 518-538. https://doi.org/10.1016/j.neuroimage.2018.03.006

Olesen, J. L., Ostergaard, L., Shemesh, N., & Jespersen, S. N. (2022). Diffusion time dependence, power-law scaling, and exchange in gray matter. *Neuroimage*, *251*, 118976. https://doi.org/10.1016/j.neuroimage.2022.118976

Palombo, M., Ianus, A., Guerreri, M., Nunes, D., Alexander, D. C., Shemesh, N., & Zhang, H. (2020). SANDI: A compartment-based model for non-invasive apparent soma and neurite imaging by diffusion MRI. *Neuroimage*, *215*, 116835. https://doi.org/10.1016/j.neuroimage.2020.116835

Palombo, M., Valindria, V., Singh, S., Chiou, E., Giganti, F., Pye, H., Whitaker, H. C., Atkinson, D., Punwani, S., Alexander, D. C., & Panagiotaki, E. (2023). Joint estimation of relaxation and diffusion tissue parameters for prostate cancer with relaxation-VERDICT MRI. *Sci Rep*, *13*(1), 2999. https://doi.org/10.1038/s41598-023-30182-1

Pasternak, O., Sochen, N., Gur, Y., Intrator, N., & Assaf, Y. (2009). Free water elimination and mapping from diffusion MRI. *Magn Reson Med*, *62*(3), 717-730. https://doi.org/10.1002/mrm.22055

Pierpaoli, C., Jezzard, P., Basser, P. J., Barnett, A., & Di Chiro, G. (1996). Diffusion tensor MR imaging of the human brain. *Radiology*, *201*(3), 637-648. https://doi.org/10.1148/radiology.201.3.8939209

Pizzolato, M., Canales-Rodriguez, E. J., Andersson, M., & Dyrby, T. B. (2023). Axial and radial axonal diffusivities and radii from single encoding strongly diffusion-weighted MRI. *Med Image Anal*, *86*, 102767. https://doi.org/10.1016/j.media.2023.102767

Reisert, M., Kellner, E., Dhital, B., Hennig, J., & Kiselev, V. G. (2017). Disentangling micro from mesostructure by diffusion MRI: A Bayesian approach. *Neuroimage*, *147*, 964-975. https://doi.org/10.1016/j.neuroimage.2016.09.058

Reisert, M., Kiselev, V. G., Dihtal, B., Kellner, E., & Novikov, D. S. (2014). MesoFT: unifying diffusion modelling and fiber tracking. *Med Image Comput Comput Assist Interv*, *17*(Pt 3), 201-208. https://doi.org/10.1007/978-3-319-10443-0_26

Salarian, A. (2024). *Intraclass Correlation Coefficient (ICC)*. In https://www.mathworks.com/matlabcentral/fileexchange/22099-intraclass-correlation-coefficient-icc

Schiavi, S., Palombo, M., Zaca, D., Tazza, F., Lapucci, C., Castellan, L., Costagli, M., & Inglese, M. (2023). Mapping tissue microstructure across the human brain on a clinical scanner with soma and neurite density image metrics. *Hum Brain Mapp*, *44*(13), 4792-4811. https://doi.org/10.1002/hbm.26416

Schiavi, S., Palombo, M., Zacà, D., Tazza, F., Lapucci, C., Castellan, L., Costagli, M., & Inglese, M. (2022). Dissecting brain grey and white matter microstructure: a novel clinical diffusion MRI protocol. *bioRxiv*, 2022.2004.2008.487640. https://doi.org/10.1101/2022.04.08.487640

Schilling, K. G., Combes, A. J. E., Ramadass, K., Rheault, F., Sweeney, G., Prock, L., Sriram, S., Cohen-Adad, J., Gore, J. C., Landman, B. A., Smith, S. A., & O'Grady, K. P. (2024).

Influence of preprocessing, distortion correction and cardiac triggering on the quality of diffusion MR images of spinal cord. *Magn Reson Imaging, 108*, 11-21. https://doi.org/10.1016/j.mri.2024.01.008

Schilling, K. G., Fadnavis, S., Batson, J., Visagie, M., Combes, A. J. E., McKnight, C. D., Bagnato, F., Garyfallidis, E., Landman, B. A., Smith, S. A., & O'Grady, K. P. (2021). Patch2Self denoising of diffusion MRI in the cervical spinal cord improves intra-cord contrast, signal modelling, repeatability, and feature conspicuity. *medRxiv*, 2021.2010.2004.21264389. https://doi.org/10.1101/2021.10.04.21264389

Schilling, K. G., O'Grady, K. P., By, S., Feiler, H., Bagnato, F., Landman, B. A., & Smith, S. A. (2021). Investigating multi-compartment diffusion MRI models in the cervical spinal cord of

multiple sclerosis patients. International Society of Magnetic Resonance in Medicine,

Schober, P., Boer, C., & Schwarte, L. A. (2018). Correlation Coefficients: Appropriate Use and Interpretation. *Anesth Analg, 126*(5), 1763-1768. https://doi.org/10.1213/ANE.0000000000002864

Snoussi, H., Caruyer, E., Cohen-Adad, J., Commowick, O., Combes, B., Bannier, E., Kerbrat, A., & Barillot, C. (2019, 8-11 April 2019). Geometric Evaluation of Distortion Correction Methods in Diffusion MRI of the Spinal Cord. 2019 IEEE 16th International Symposium on Biomedical Imaging (ISBI 2019),

Snoussi, H., Cohen-Adad, J., Commowick, O., Combes, B., Bannier, E., Leguy, S., Kerbrat, A., Barillot, C., & Caruyer, E. (2021). Evaluation of distortion correction methods in diffusion MRI of the spinal cord. *arXiv preprint arXiv:2108.03817*.

Song, S. K., Sun, S. W., Ramsbottom, M. J., Chang, C., Russell, J., & Cross, A. H. (2002). Dysmyelination revealed through MRI as increased radial (but unchanged axial) diffusion of water. *Neuroimage, 17*(3), 1429-1436. https://www.ncbi.nlm.nih.gov/pubmed/12414282

Sotiropoulos, S. N., Behrens, T. E., & Jbabdi, S. (2012). Ball and rackets: Inferring fiber fanning from diffusion-weighted MRI. *Neuroimage, 60*(2), 1412-1425. https://doi.org/10.1016/j.neuroimage.2012.01.056

Tournier, J. D., Smith, R., Raffelt, D., Tabbara, R., Dhollander, T., Pietsch, M., Christiaens, D., Jeurissen, B., Yeh, C. H., & Connelly, A. (2019). MRtrix3: A fast, flexible and open software framework for medical image processing and visualisation. *Neuroimage, 202*, 116137. https://doi.org/10.1016/j.neuroimage.2019.116137

Ullmann, E., Pelletier Paquette, J. F., Thong, W. E., & Cohen-Adad, J. (2014). Automatic labeling of vertebral levels using a robust template-based approach. *Int J Biomed Imaging, 2014*, 719520. https://doi.org/10.1155/2014/719520

Vedantam, A., Jirjis, M. B., Schmit, B. D., Wang, M. C., Ulmer, J. L., & Kurpad, S. N. (2014). Diffusion tensor imaging of the spinal cord: insights from animal and human studies. *Neurosurgery, 74*(1), 1-8; discussion 8; quiz 8. https://doi.org/10.1227/NEU.0000000000000171

Veraart, J., Fieremans, E., & Novikov, D. S. (2016). Diffusion MRI noise mapping using random matrix theory. *Magn Reson Med, 76*(5), 1582-1593. https://doi.org/10.1002/mrm.26059

Veraart, J., Fieremans, E., & Novikov, D. S. (2019). On the scaling behavior of water diffusion in human brain white matter. *Neuroimage*, *185*, 379-387. https://doi.org/10.1016/j.neuroimage.2018.09.075

Veraart, J., Novikov, D. S., Christiaens, D., Ades-Aron, B., Sijbers, J., & Fieremans, E. (2016). Denoising of diffusion MRI using random matrix theory. *Neuroimage*, *142*, 394-406. https://doi.org/10.1016/j.neuroimage.2016.08.016

Veraart, J., Nunes, D., Rudrapatna, U., Fieremans, E., Jones, D. K., Novikov, D. S., & Shemesh, N. (2020). Nonivasive quantification of axon radii using diffusion MRI. *Elife*, *9*. https://doi.org/10.7554/eLife.49855

Veraart, J., Raven, E. P., Edwards, L. J., Weiskopf, N., & Jones, D. K. (2021). The variability of MR axon radii estimates in the human white matter. *Hum Brain Mapp*, *42*(7), 2201-2213. https://doi.org/10.1002/hbm.25359

Williamson, N. H., Ravin, R., Benjamini, D., Merkle, H., Falgairolle, M., O'Donovan, M. J., Blivis, D., Ide, D., Cai, T. X., Ghorashi, N. S., Bai, R., & Basser, P. J. (2019). Magnetic resonance measurements of cellular and sub-cellular membrane structures in live and fixed neural tissue. *Elife*, *8*. https://doi.org/10.7554/eLife.51101

Wilm, B. J., Svensson, J., Henning, A., Pruessmann, K. P., Boesiger, P., & Kollias, S. S. (2007). Reduced field-of-view MRI using outer volume suppression for spinal cord diffusion imaging. *Magn Reson Med*, *57*(3), 625-630. https://doi.org/10.1002/mrm.21167

Xu, J., Shimony, J. S., Klawiter, E. C., Snyder, A. Z., Trinkaus, K., Naismith, R. T., Benzinger, T. L., Cross, A. H., & Song, S. K. (2013). Improved in vivo diffusion tensor imaging of human cervical spinal cord. *Neuroimage*, *67*, 64-76. https://doi.org/10.1016/j.neuroimage.2012.11.014

Zhang, H., Schneider, T., Wheeler-Kingshott, C. A., & Alexander, D. C. (2012). NODDI: practical in vivo neurite orientation dispersion and density imaging of the human brain. *Neuroimage*, *61*(4), 1000-1016. https://doi.org/10.1016/j.neuroimage.2012.03.072